

Indoor Light and Heat Estimation from a Single Panorama

Guanzhou Ji^a, Sriram Narayanan^a, Azadeh O. Sawyer^a,
and Srinivasa G. Narasimhan^a

^aCarnegie Mellon University, Pittsburgh, PA, USA

ARTICLE HISTORY

Compiled February 12, 2025

ABSTRACT

This paper presents a novel application for directly estimating indoor light and heat maps from captured indoor-outdoor High Dynamic Range (HDR) panoramas. In our image-based rendering method, the indoor panorama is used to estimate the 3D room layout, while the corresponding outdoor panorama serves as an environment map to infer spatially-varying light and material properties. We establish a connection between indoor light transport and heat transport and implement transient heat simulation to generate indoor heat panoramas. The sensitivity analysis of various thermal parameters is conducted, and the resulting heat maps are compared with the images captured by the thermal camera in real-world scenarios. This digital application enables automatic indoor light and heat estimation without manual inputs and cumbersome field measurements.

KEYWORDS

Indoor Scene; Light Estimation; Heat Estimation; Image-Based Rendering; HDR
Photography

1. Introduction

Outdoor light enters indoor spaces, shapes the appearance of indoor scenes, and brings solar radiation that generates heat on indoor surfaces. Omnidirectional photography has been used to capture panoramic images of entire indoor scenes. Based on physics-based and data-driven methods (Ji et al. (2023, 2024); Zhi et al. (2022)), a single indoor panorama can be directly used to estimate spatially varying indoor lighting, material properties, and 3D layouts. Estimating indoor light levels allows users to identify optimal areas for activities, while heat estimation helps assess the potential heating and cooling demand for the entire space. However, most thermal imaging relies on infrared thermal cameras, which are expensive, output noisy imaging results, and are limited to capturing 2D perspective images, making it challenging to cover an entire 360° indoor scene in high quality. This raises a main research question: Can we estimate indoor lighting and heating properties simultaneously from a single indoor panorama?

The global rendering method proposed by Debevec (2006) offers a High Dynamic Range (HDR) image-based rendering model for relighting virtual objects within a realistic scene context. Virtual sky models (CIE (2003); Perez et al. (1993); Hosek and

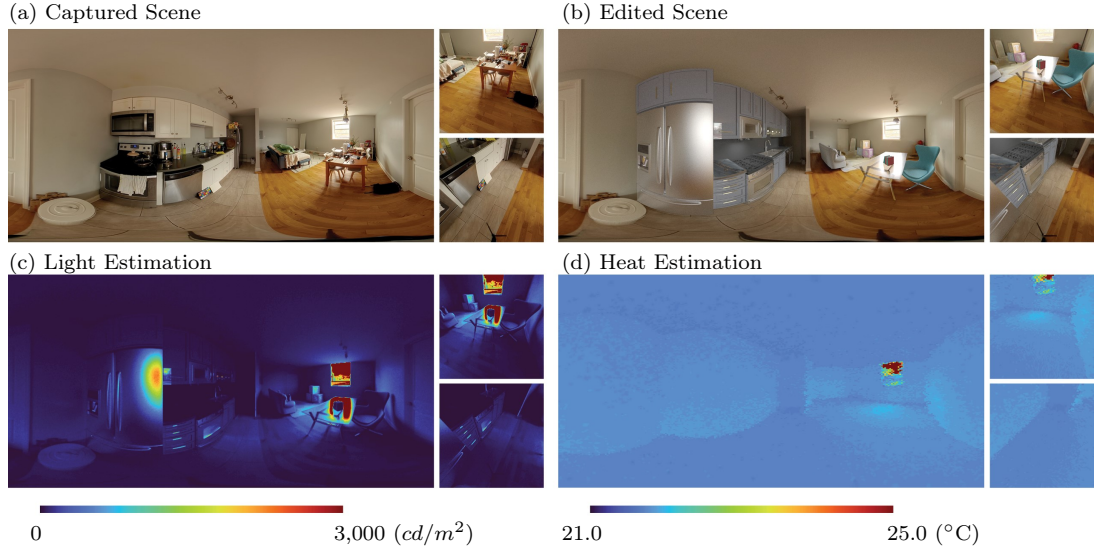


Figure 1.: Overview of Our Application: An indoor panorama (a) is captured under natural illumination, with a paired outdoor panorama providing real-time, spatially-varying light to the scene. The scene is virtually edited and relit with new indoor layout objects (b). The absolute light level is estimated for the virtual scene, and we introduced a heat transport equation to compute an indoor heat map displaying per-pixel temperature values.

Wilkie (2012)) have been employed to represent outdoor light in the real world. To reflect instantaneous light estimation for indoor scenes, image-based rendering incorporates realistic sky images as the illumination source. The HDR technique captures the sky appearance, including direct sunlight in outdoor spaces (Stumpfel et al. (2004)). The captured HDR images provide accurate sky luminance distribution and details of the urban context (Inanici (2009, 2010)). In this setting, the indoor scene is accurately rendered using the outdoor sky image at the pixel level. However, so far, the image-based rendering method has not been explored with realistic indoor textures to render photorealistic indoor appearances to estimate absolute light levels and heat maps.

When modeling visible light transport, intrinsic decomposition separates a single image into two layers: a reflectance layer, which captures the material surface’s albedo or color invariant, and a shading layer, which is shaped by light interactions and object geometry. Intrinsic decomposition has been applied in various tasks, including image editing (Bonneel et al. (2017)), removing interreflections (Seitz et al. (2005)), and separating illumination for material recoloring (Carroll et al. (2011)), as well as being applied to multi-view outdoor photos (Duchêne et al. (2015)). To construct indoor-outdoor light transport, Ji et al. (2023, 2024) use an indoor panorama and paired outdoor hemispherical image to virtually render existing scenes with new floor layouts, materials, and illumination conditions. In this study, we estimate the absolute light levels in virtual indoor scenes by modeling light transport using paired indoor and outdoor panoramas. This approach offers an efficient method for accurately simulating indoor illumination conditions.

Heat transport includes the process of heat generated by the source and its exchange between different mediums (Bergman et al. (2011)). Temperature exchange within an object follows the well-known heat transfer physics, and three primary mechanisms

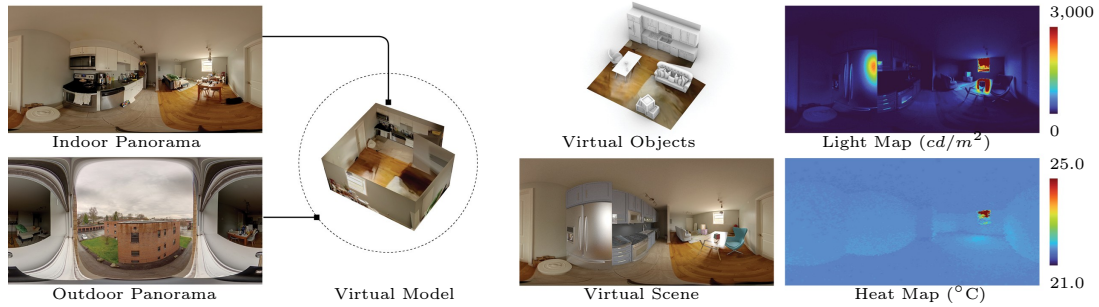


Figure 2.: Overview of Our Application: First, a single camera (Ricoh Theta Z1) captures paired indoor and outdoor panoramas. Second, the indoor panorama is used to estimate the 3D floor layout, while the outdoor panorama provides a 360° environment map for the virtual model. Third, virtual objects are inserted into the scene, and the objects are relit within the scene. Finally, an indoor light map with absolute light level (cd/m^2) and a heat map ($^{\circ}C$) are computed for the room.

include conduction, convection, and radiation. Recent work by Ramanagopal et al. (2024) bridges visible light transport and heat transport in solids and estimates the heat generation from light absorption. Previous studies on heat estimation have primarily focused on small objects under controlled, artificial lighting and captured thermal images in a 2D perspective. In this work, by determining the reflectance properties of indoor materials from captured indoor-outdoor images, the amount of heat absorbed can be estimated.

In this work, we proposed a digital application that exploits paired indoor-outdoor HDR panoramas as input and then estimates indoor lighting and heating properties in panoramic representation (Fig. 2). This work demonstrates that indoor heat generated by light absorption can be estimated by modeling heat transport using a forward rendering process. This work makes the following technical contributions:

- (1) An image-based rendering approach using paired indoor-outdoor panoramas to estimate indoor materials, 3D geometry, and lighting for physics-based building analysis.
- (2) An application for computing the absolute light level for indoor visual tasks and scene design.
- (3) An application for estimating indoor heat map by implementing the transient heat equation.
- (4) Parametric analysis is conducted under varying thermal parameters for the transient heat simulation, and the resulting virtual heat maps are compared with real-world thermal images.

2. Related Work

2.1. Indoor Light Estimation

Directly estimating indoor light from an indoor image is an ill-posed problem. Under natural illumination, the indoor spatially-varying light depends on the outdoor context, scene geometry, and material properties. Given a 2D perspective image, some

studies focus on predicting panoramic HDR environment maps (Gardner et al. (2017)), lighting representation (Gardner et al. (2019)), and estimating HDR panoramas from LDR images (Gkitsas et al. (2020); LeGendre et al. (2019); Gardner et al. (2017)). Extensive research efforts have been devoted to estimating HDR from LDR images using inverse tone mapping algorithms (Rempel et al. (2007); Banterle et al. (2006, 2007); Reinhard et al. (2002)). The estimated HDR panorama is used as a global light source for high-quality relighting and inserting new virtual 3D objects into the scene. Previous studies have also explored indoor lighting editing (Li et al. (2022)), material property estimation (Yeh et al. (2022)), and recovery of spatially-varying lighting (Li et al. (2020); Garon et al. (2019); Srinivasan et al. (2020)) from images. User inputs provide additional information to define scene geometry and light location and direction (Karsch et al. (2011)). Through user-annotated light positions, Zhang et al. (2016) recover indoor illumination and room geometry from a complete RGB-D scan of a scene.

Since the input 2D perspective image is in LDR format, while the estimated HDR environment map from previous work serves as a global light source, it often fails to recover the accurate scene radiance of the real world. More importantly, earlier studies that directly estimate environment maps from images do not construct a complete light transport model. Such a model would ideally account for outdoor lighting, scene geometry, and material properties and present a complete interaction between light and the environment.

2.2. Outdoor Light Estimation

Outdoor light changes with the appearance of the sky, the surrounding context, and the time of day. The luminance and angular distribution of the sky also vary with cloud levels, times of year, and geographic locations. Perez sky model (Perez et al. (1993)) and the CIE standard sky model (CIE (2003)) are commonly used to estimate outdoor light. Due to the nuanced difference between cloud cover and sunlight intensity, generalized sky models cannot fully describe the realistic sky appearance (Darula and Kittler (2002)). Recent studies have focused on estimating the appearance of the spectral sky. A spectral sky represents chromatic changes based on time, sky turbidity, and geographic locations (Hosek and Wilkie (2012)). Furthermore, analytical sky models (Lalonde et al. (2012); Preetham et al. (1999)) approximate full-spectrum daylight under various atmospheric conditions.

In addition to generating sky model images, some studies aim to estimate outdoor lighting directly from 2D images. Learning-based method estimates 360° outdoor environment map from a single 2D photograph (Hold-Geoffroy et al. (2017); Lalonde and Matthews (2014)). Lalonde and Matthews (2014) developed a method to estimate light direction and intensity from a single Low Dynamic Range (LDR) image, and the generated HDR sky models are used for relighting new objects. Zhang and Lalonde (2017) recover linear HDR outdoor images from a single LDR panorama. Sunkavalli et al. (2008) recover time-varying color variation for the outdoor scene under direct sunlight and ambient skylight. The recent study by Dastjerdi et al. (2023) directly adds, removes, and edits the indoor and outdoor illumination sources in the panoramic representation. However, those studies focus on estimating outdoor environment maps for relighting new virtual objects; the outdoor light source is not used to estimate indoor light transport.

2.3. Thermal Imaging Technique

Above absolute zero temperature, indoor objects radiate infrared energy in the Long-Wave Infrared (LWIR) spectrum (wavelengths between 8 μm and 15 μm), resulting in heat on the object’s surface. The radiometric quantity of the heat transfer can be measured by infrared thermal imaging technique (Holst (2000); Kaplan (2007); Vollmer (2020); Planinsic (2011)). Thermal imaging has gained increasing attention in computer vision research and leads to applications based on the thermal spectrum, such as object segmentation (Huo et al. (2023)), 3D estimation (Eren et al. (2009); Shin et al. (2023); Narayanan et al. (2025)), and material property estimation (Dashpute et al. (2023)).

Thermography has been extensively used to collect surface heat in building spaces. In outdoor applications, recent studies have focused on identifying thermal leakage on exterior facades (Motayyeb et al. (2023)) and integrating thermal attributes with 3D point clouds (Jarzabek-Rychard et al. (2020)). In indoor scenarios, recent research has combined 3D point clouds with 2D thermography for generating 3D building models (Adán et al. (2017); Schmoll et al. (2022)), detecting faults on interior surfaces (Garrido et al. (2018)), and segmenting targeted thermal regions on building surfaces (Adán et al. (2020)). Additionally, heat maps can be captured by a thermal-infrared camera from multiple indoor locations to analyze the heat generated on vertical wall planes (López-Fernández et al. (2017)), support 3D modeling (Adán et al. (2017)), and combine with RGB-D camera for spatial mapping (Vidas et al. (2013)).

Existing studies on indoor thermography primarily focus on capturing temporal heat maps at specific time points. There are several limitations. First, 2D thermography captures only a limited field of view. Second, capturing multiple 2D perspective images requires additional effort in data post-processing, such as image registration and alignment. Third, implementing infrared thermal cameras with additional devices like RGB-D cameras or LiDAR adds complexity and increases data acquisition costs.

3. Methodology

3.1. Indoor Light Estimation

Using a single panorama, scene editing enables users to modify the indoor camera position, adjust lighting conditions, and change materials. Fig. 3 illustrates a reading scenario and shows the effects of indoor changes with three desk materials: glass, marble, and wood. Beyond the RGB image, the absolute light level is crucial for indoor daily activities. The virtual scene is rendered in HDR format and then converted into luminance values through per-pixel computation (Fig. 4). Since both indoor and outdoor HDR images are calibrated to accurately represent real-world scene radiance, this process ensures that the luminance value (cd/m^2) in the virtual rendered scene is accurately estimated through physics-based rendering.

3.2. Indoor Task Lighting

In addition to luminance (scene radiance), illuminance (scene irradiance) is commonly used to evaluate the adequacy of indoor task lighting. Each indoor task has its own specific target light level to ensure optimal lighting conditions. To convert and obtain the illuminance map, we assume the scene object is Lambertian surface, where the reflectance (R) of the diffuse scene materials are known. The global illuminance map can be derived from displayed luminance value on HDR image (Yang et al. (2013)).

The conversion of Illuminance (E) (lx) from Luminance (L) (cd/m^2) is:

$$E = \frac{L\pi}{R} \quad (1)$$

The indoor task is visualized from a 180° hemispherical fisheye perspective. Fig. 5 showcases a virtual scene for a reading task. When the desk in the original scene is repositioned to face the wall, and a new desk lamp and ceiling light are added to illuminate the scene, the luminance levels in the virtual scenes can be estimated from the virtual HDR image. Based on the Lambertian assumption for the scene, the average illuminance level on the desk surface can be calculated. If the reading task requires a target brightness of $300\ lux$, a code-based compliance analysis computes the error map to evaluate whether the light is above or below the target level for the reading task.

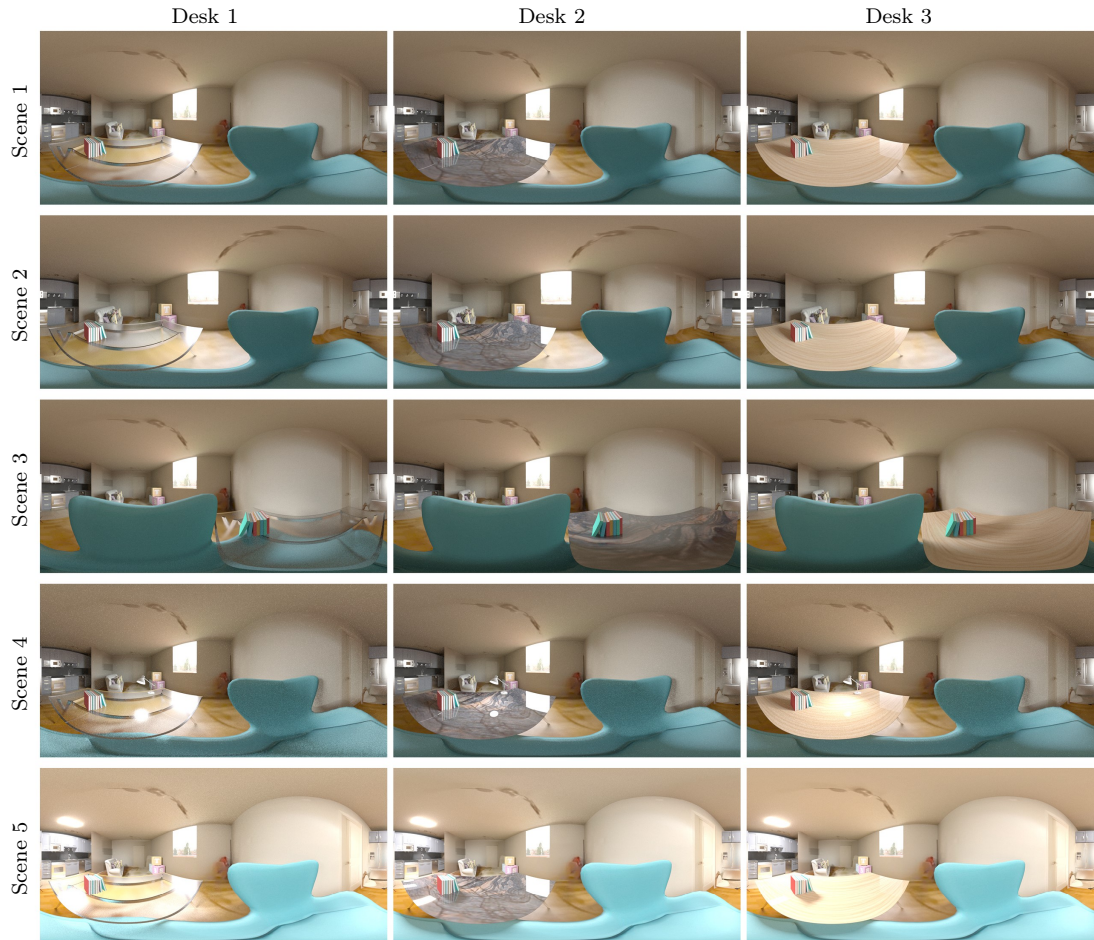


Figure 3.: Examples of indoor lighting analysis with new indoor layouts and lighting conditions. Three desks are added to the scene. Scene 1 shows the original reading scenario. Scene 2 depicts the desks and chairs moved closer to the couch. Scene 3 shows the desks repositioned to face the wall. Scene 4 features the addition of a desk lamp as an extra light source. Scene 5 includes a ceiling light mounted on the ceiling.

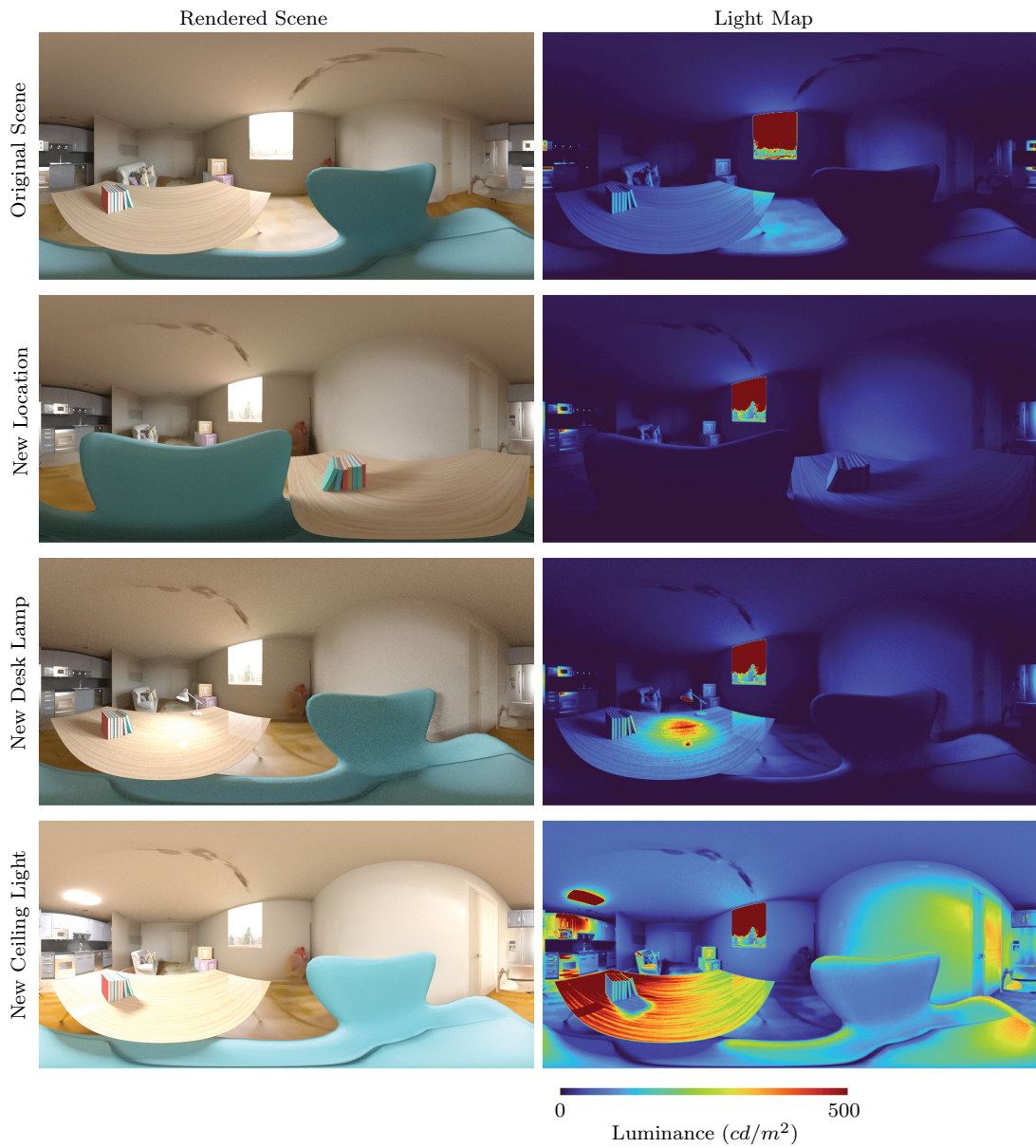


Figure 4.: Estimating indoor absolute light levels from virtual rendered scenes. The original scene depicts a reading scenario with a desk and chair within the field of view. The scene is edited with a new desk location, a new desk lamp, and a new ceiling light. The light map displays the absolute luminance values (cd/m^2) for the corresponding scenes.

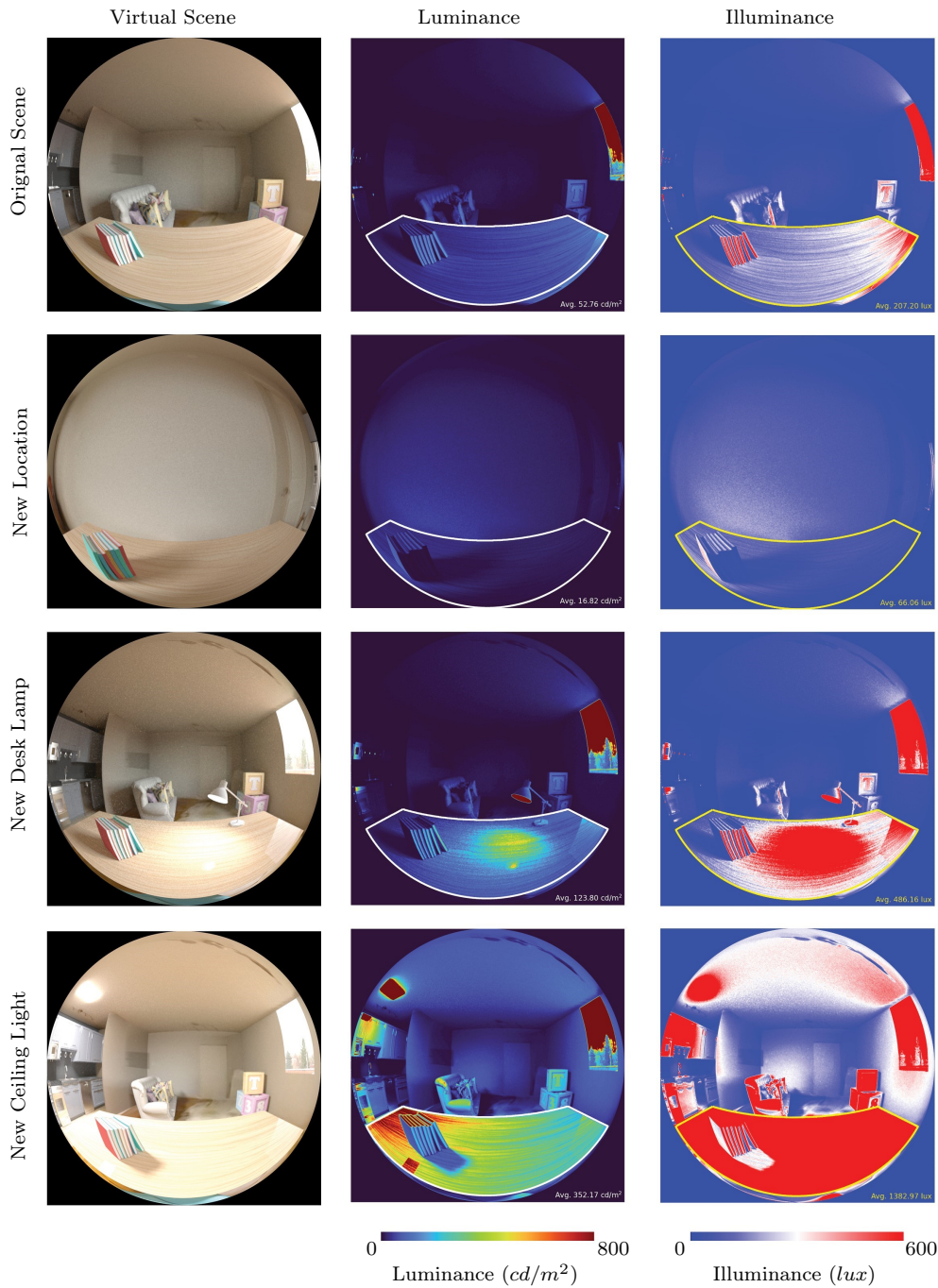


Figure 5.: Estimating indoor absolute luminance (cd/m^2) and illuminance (lux) levels from virtual rendered scenes. The original scene depicts a reading scenario with a desk and chair within the field of view. The scene is edited with a new desk location, a new desk lamp, and a new ceiling light.

4. Indoor Heat Estimation

The heat estimation requires absolute energy influx for each indoor location. As shown in Fig. 6, we rendered the existing scene in HDR format and then used per-pixel computation to convert it into the corresponding luminance map. Typically, converting illuminance to energy influx requires specialized measurement equipment. Because we focus on the indoor scene under natural light, the per-pixel energy influx can be approximated directly from the illuminance values (obtained from Equ. 1). In indoor settings, an engineering conversion suggests that 120 lux is approximately equivalent to 1 W/m^2 for sunlight (Michael et al. (2020)). As shown in Fig. 6, the energy influx, converted from the indoor luminance map, will be used as an absolute heat source to compute the indoor heat map.

4.1. Transient Heat Simulation

Heat on indoor surfaces varies over time, influenced by material properties (like thermal conductivity, density, and thickness), heat capacity, and surrounding temperatures. We aim to implement a transient heat transport equation to estimate the heat generated by natural light over time.

Thermal diffusivity (α) of a material can be expressed as:

$$\alpha = \frac{k}{\rho c_p} \quad (2)$$

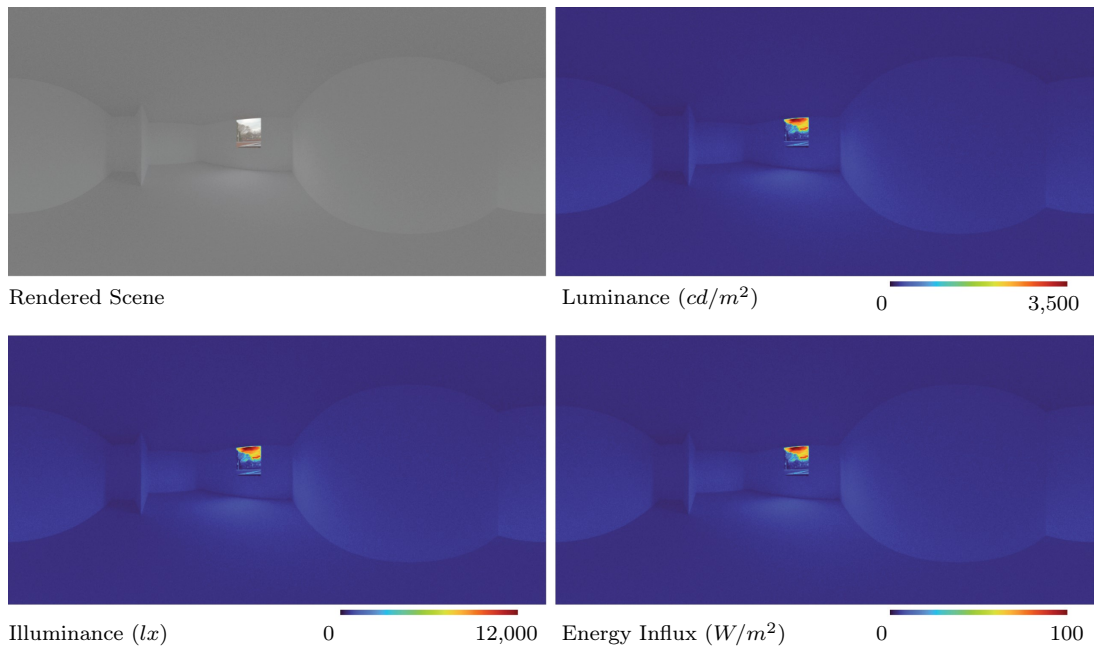


Figure 6.: Conversion between Lighting and Energy Influx. The scene is rendered in HDR format (upper left) and converted into a luminance map (upper right). Assuming a Lambertian surface for the 3D scene, the illuminance map (bottom left) is derived from the luminance map, enabling an approximation of the absolute energy influx (bottom right).

Where k is the thermal conductivity of the material ($W/m \cdot K$), ρ is the density of the material (kg/m^3), and c_p is the specific heat capacity of the material at constant pressure ($J/(kg \cdot K)$). The indoor scene has a wide range of building materials, and those variables can be accessed from the existing material database (IESVE (2018)).

Intrinsic attributes, such as the Laplace operator, are fundamental quantities in various physical simulations, including heat transfer. The work by Narayanan et al. (2025) estimates intrinsic 3D shapes from thermal videos, where transient heat transport follows:

$$\frac{dT}{dt} = \alpha \Delta T + \mathbb{1}_{\partial\Omega} \frac{1}{\rho c_p dV} \left(\sigma \epsilon A (T_{surr}^4 - T^4) + h_c A (T_{surr} - T) + A \beta \phi_q \right) \quad (3)$$

The first term ΔT represents conduction, and the second term represents the sum of radiation, convection, and input heat source; other quantities are explained in Table 1.

The Equ. 3 applies to the object heated by three transfer approaches given the surrounding temperature. For indoor surfaces, heat changes not only by spatially-varying light distribution but also by heat transfer between indoor and outdoor spaces. Therefore, we include heat exchange between indoor and outdoor spaces in the heat equation and add outdoor temperature (T_{out}) into the heat transport equation:

$$\frac{dT}{dt} = \alpha \Delta T + \mathbb{1}_{\partial\Omega} \frac{1}{\rho c_p dV} \left(\sigma \epsilon A (T_{surr}^4 - T^4) + h_c A (T_{surr} - T) + A \beta \phi_q + A (T - T_{out}) \right) \quad (4)$$

Table 1.: Properties, descriptions, and units for the variables in the Eq. 2, Eq. 3, and Eq. 4.

Property	Description	Unit
h_c	Convection coefficient	$W/(m^2 \cdot K)$
k	Thermal conductivity of the material	$W/m \cdot K$
ρ	Density of the material	kg/m^3
c_p	Specific heat capacity	$J/(kg \cdot K)$
ϵ	Emissivity	–
β	Energy absorption factor	–
ϕ_q	Input heat flux density	W/m^2
A	Surface area	m^2
σ	Stefan-Boltzmann constant	$W/(m^2 K^4)$
T	Temperature	K
T_{surr}	Surrounding temperature	K
T_{out}	Outdoor temperature	K
α	Thermal diffusivity	m^2/s

We estimate the indoor heat map using the transient heat equation to calculate the temperature at each pixel. In Fig. 7, the 3D floor layout is derived from a single indoor panorama. The heat simulation is conducted in 3D coordinates, with planar surfaces

subdivided into vertices to compute the heat value for each point. After the simulation, the heat data in 3D coordinates is mapped onto an equirectangular projection and displayed on a panorama with the same camera position as the input panorama.

The transient heat simulation allows the heat values to be visualized over time. In Fig. 8, we selected a scene to estimate heat changes on the 3D layout from a top-down perspective. The results of the heat simulation are recorded at time steps, where the 0s figure shows the indoor space at the initial temperature. As time progresses, the indoor space heats up, and the indoor temperature is captured incrementally at each step.

Our application can estimate indoor light and heat panoramas based on new outdoor images. In Fig. 9, the existing scene is rendered under real-time outdoor lighting at 13:48. We virtually edited the sun’s position to simulate different times and estimated the corresponding panoramic heat map. In Fig. 10, we present the joint estimation of indoor light and heat properties within the scene. The existing scene is renovated with new furniture objects and then converted into the corresponding light and heat maps. Following the approach by Ji et al. (2024), the outdoor scene is initially cloudy, and direct sunlight is added to the outdoor image and used as a light source to relight the scene at different times in the afternoon (16:45, 17:45, and 18:45). In contrast to the cloudy day scenario, increased direct sunlight enters the indoor space, intensifying illumination on the table and walls while producing strong reflections on the refrigerator. This direct sunlight also raises the temperature levels on the wall and floor surfaces near the window.

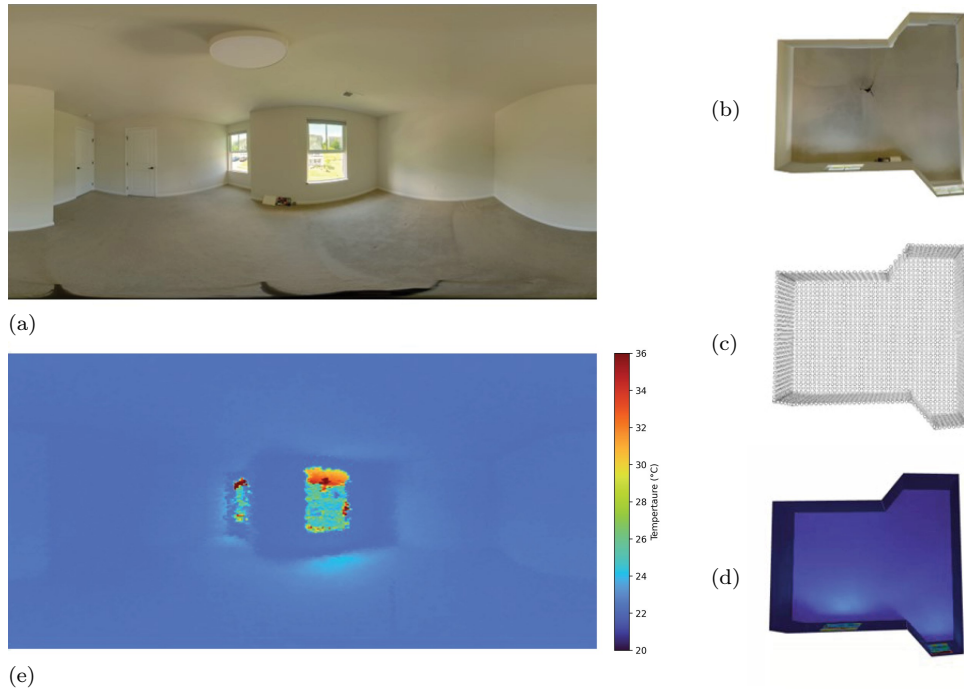


Figure 7.: Heat Simulation Process. (a) The input is a single panorama, (b) a 3D layout is estimated from the input panorama, (c) a grid of vertices is generated from the planar mesh objects, (d) the heat equation is applied to compute the per-pixel heat value for each vertice, and (e) the output is the heat map converted from 3D coordinate into equirectangular representation for this scene.

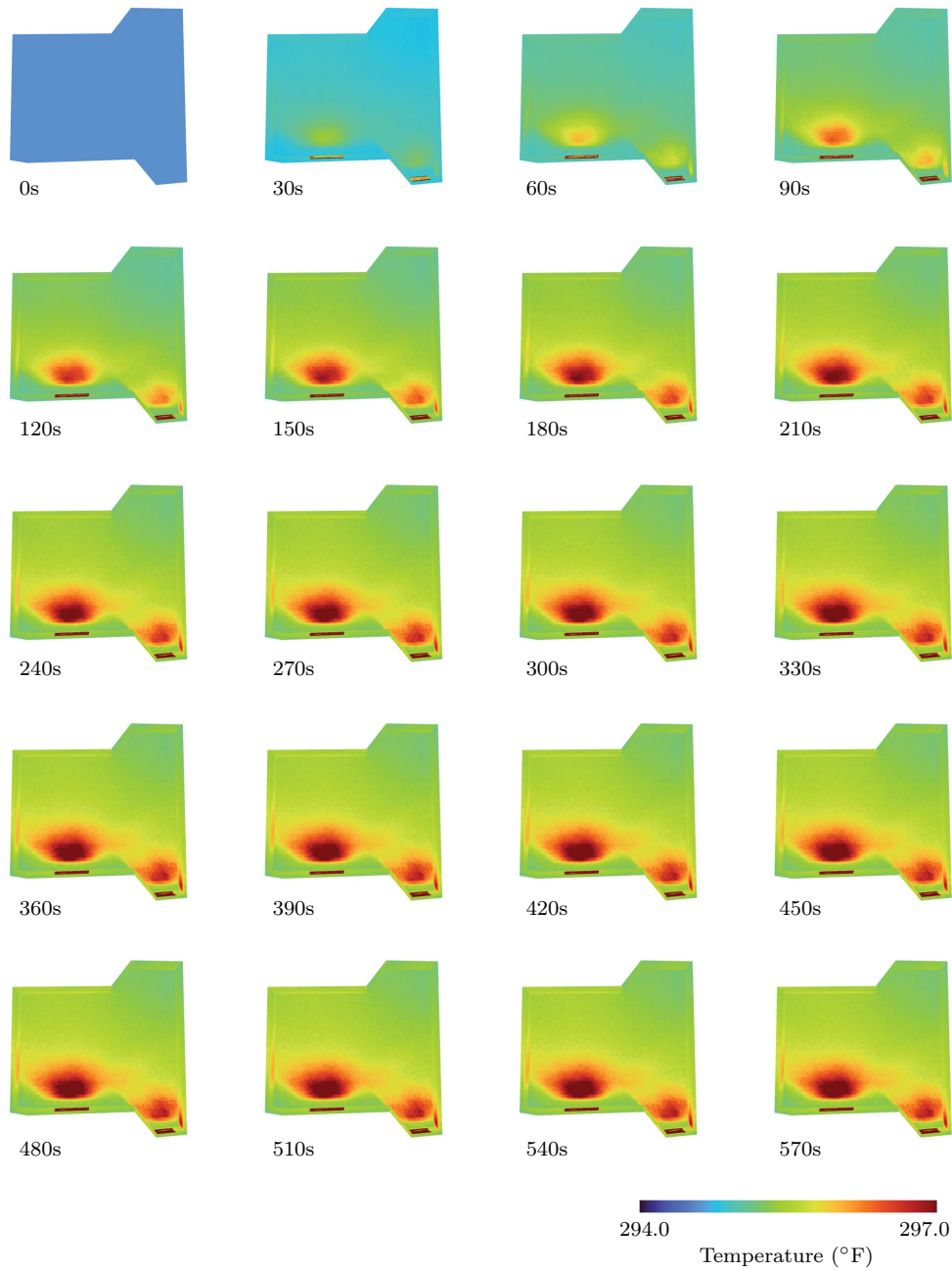


Figure 8.: Transient heat simulation over time. The heat map is initialized and recorded at each time step, displayed from a top-down perspective to illustrate the 3D floor layout as the heat changes from 0s to 570s.

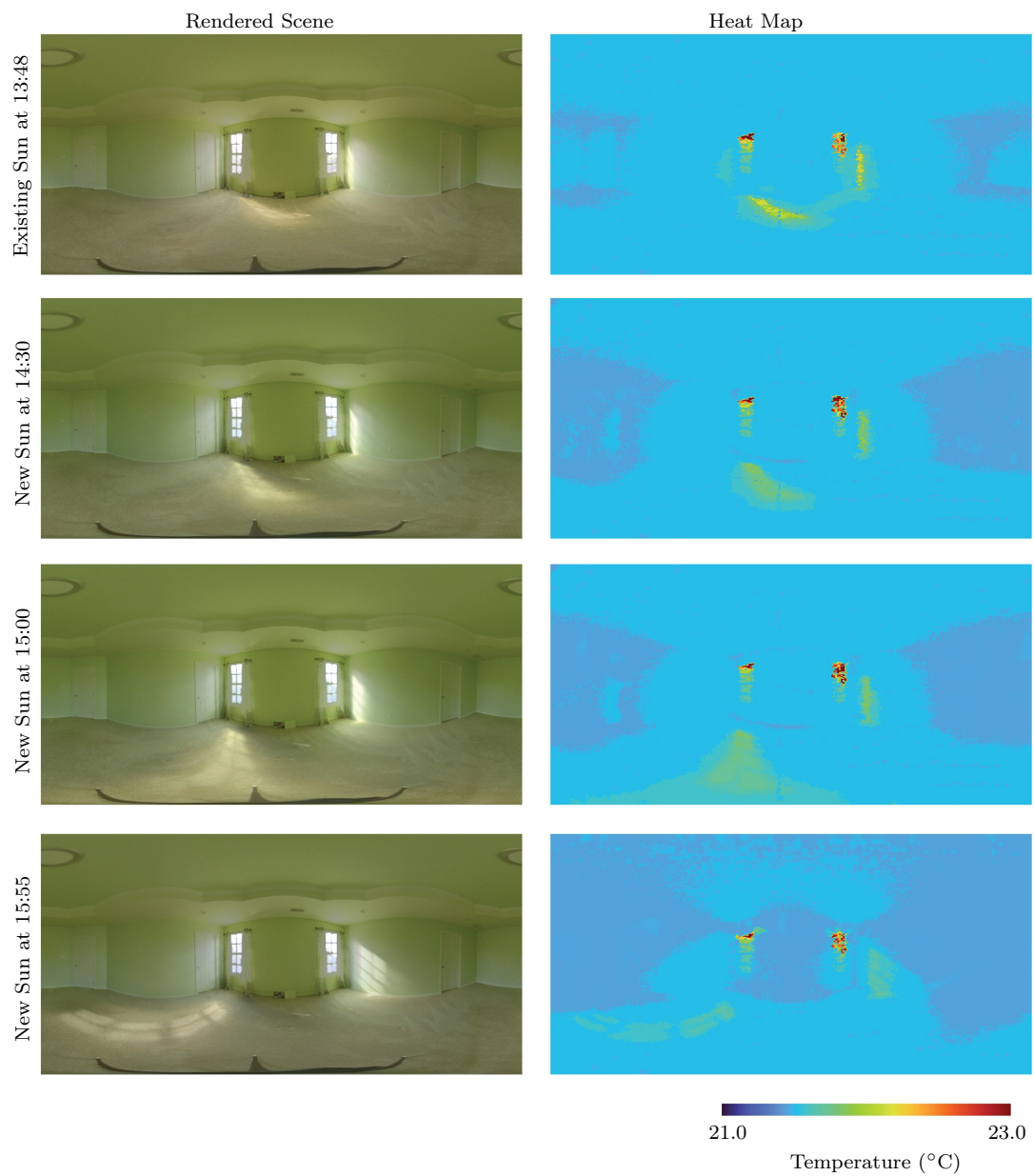


Figure 9.: Estimating indoor heat map at different times. The top row shows the scene rendered with the existing outdoor image with clear sky condition at 13:48. Subsequent rows showcase the scene rendered with the new virtual sun positions and their corresponding heat maps at 14:30 (second row), 15:00 (third row), and 15:55 (bottom row).

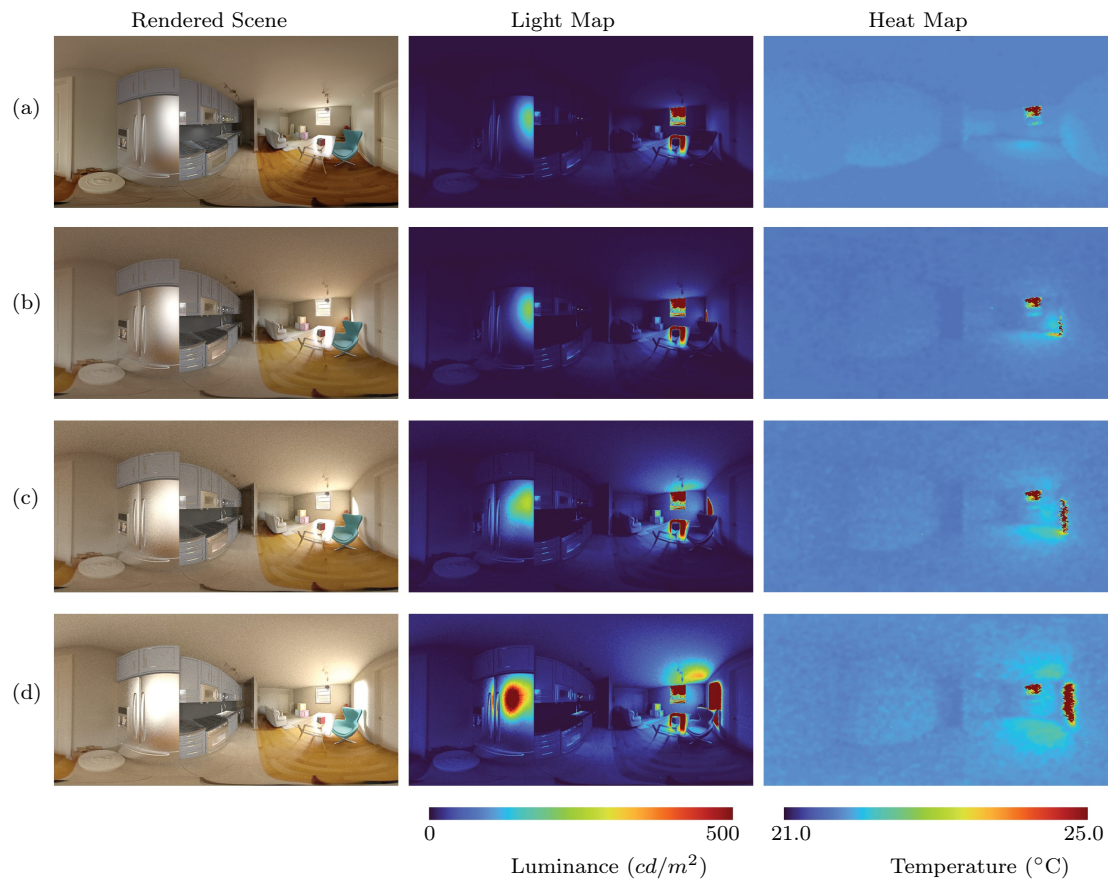


Figure 10.: Indoor Light and Heat Estimation Under New Outdoor Sun Illuminations: (a). The virtual scene is rendered under the captured outdoor panorama. (b) The virtual scene is rendered with direct sun illumination at 16:45 (b), 17:45 (c) and 18:45 (d), respectively.

4.2. Sensitivity Analysis

The transient heat simulation (Equ. 3) accounts for three types of heat transfer: conduction, radiation, and convection. To evaluate the impact of each component on heat estimation, parametric heat simulations were performed with various combinations of these components, and corresponding heat maps for each condition are visualized, as shown in Fig. 11. When conduction, radiation, and convection are all included, the resulting heat map is considered the baseline for computing the error map. When there is no heat transfer (such as conduction, radiation, and convection), the temperature remains at its highest, as no heat is emitted from the object’s surface. Adding different types of heat transfer results in varying reductions in surface temperature. Each heat map is compared with the baseline image. In the error map, the first row shows a matrix with zero values, which indicates no temperature difference. Due to the low material conductivity in this simulation, the third row exhibits minimal temperature differences. Other combinations of heat transfer mechanisms increase the temperature by varying degrees, highlighting their individual and collective contributions to the heat distribution.

Various physical parameters in the heat simulation are analyzed for their impacts on indoor surface temperature. For a single panorama, we developed a graphic user interface (GUI) that allows users to click on the input image and outline circular target areas within indoor scenes. These selected target patches are used to compute the average temperature over their coverage, as shown in Fig. 12. We selected standard materials and parameters to generate the corresponding indoor heat maps. The default heat simulation time is 600s, the surface thickness is 1mm, and the indoor ambient temperature is 21.11°C.

For different surface materials (Fig. 13), the surface temperatures and temperature differences (using the temperatures under plaster dense as baseline values) are visualized. Copper results in the lowest temperature on indoor surfaces, while plaster-dense, polystyrene, PVC (polyvinyl chloride), and simulated sheep wool result in higher temperatures than other materials and display similar temperature values across indoor surfaces.

Each material has its unique density, conductivity, and specific heat capacity. In this step, we set the default material to plaster-dense, adjust a single material property, and analyze its impact on surface temperature. Temperatures under different material densities and temperature differences (using the temperatures under correct density (1300 kg/mm^3) as baseline values) are visualized (Fig. 14). We observe that, as material density (kg/mm^3) increases, surface temperature decreases in general. While some temperatures rise on ceilings under 3300 and 5300 kg/mm^3 , with increments in material density, the temperatures at 1200, 1250, 1300, 1350, 1400, and 1500 kg/mm^3 are identical. When the material density reaches 7300 kg/mm^3 , it decreases the surface temperature by approximately between - 0.27 and 0.36 °C, with a corresponding percentage error between -1.00 and -1.60 %.

When changing material conductivity and specific heat capacity values, the surface temperature on indoor surfaces did not show differences (Fig. 15). This suggests that, compared to material density, conductivity and heat capacity have minor impacts on surface temperature when using plaster-dense as the material and our default simulation settings. While additional simulations could be conducted to further investigate this pattern, this section primarily focuses on the standard building materials and changes their thermal properties in the transient heat simulation.

Surface thickness is crucial in heat simulation, as thicker materials contain more



Figure 11.: The Effects of Three Heat Transfer Types in Heat Simulations (Equation 3). Black dots indicate when a heat transfer type is toggled. The first three columns show component combinations. Heat maps display simulation results for each combination, while error maps compare results to the first row (all components active), where the error is zero. Minimal conduction effects, due to low material conductivity (Plaster: $0.5 \text{ W}/(m \cdot K)$), result in minor differences in the third-row error map.

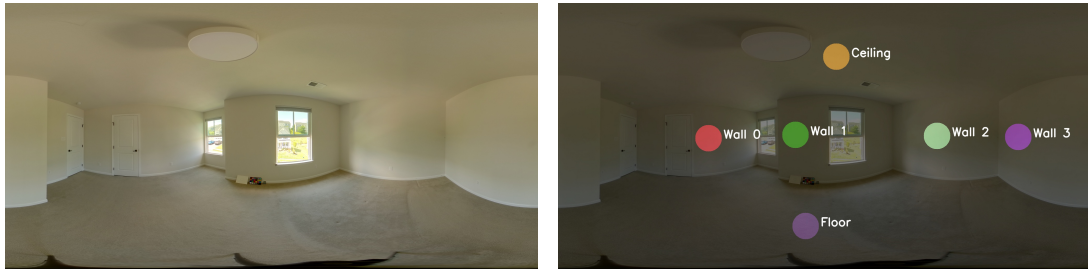


Figure 12.: (Left) An indoor panorama. (Right) The target patches are selected by user mouse clicks, which will be used to compute the average temperature in each patch.

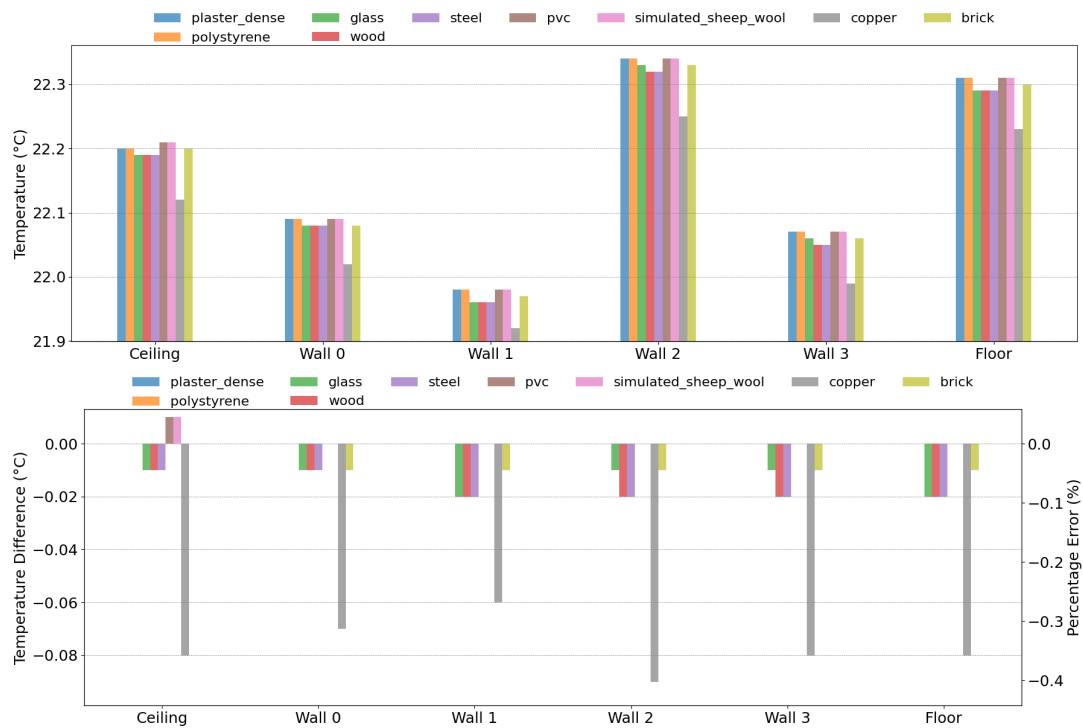


Figure 13.: (Top) The average temperature on indoor surfaces under different materials types. (Bottom) Using the temperature values under plaster dense as baseline values to compute the temperature difference (°C) and percentage error (%).

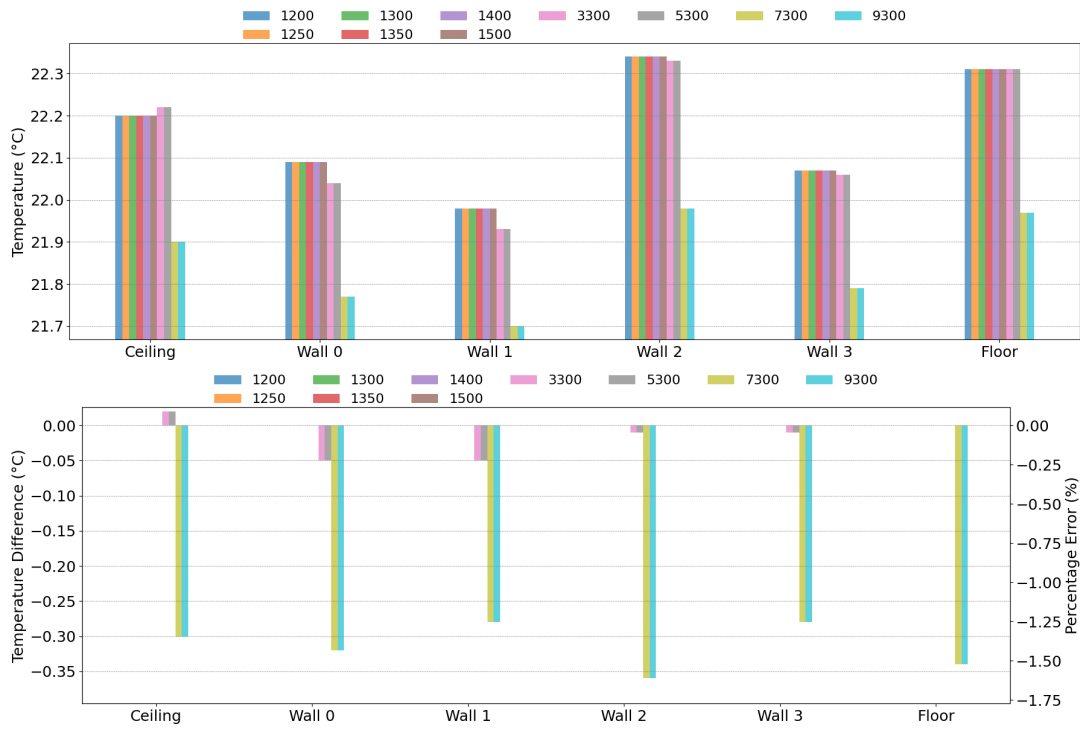


Figure 14.: (Top) The average temperature of indoor surfaces under different material density values (kg/mm^3): 1200, 1250, 1300, 1350, 1400, 1500, 3300, 5300, 7300, and 9300. (Bottom) Using the temperature values at the correct density of 1300 as baseline values to compute the temperature difference ($^{\circ}C$) and percentage error (%).

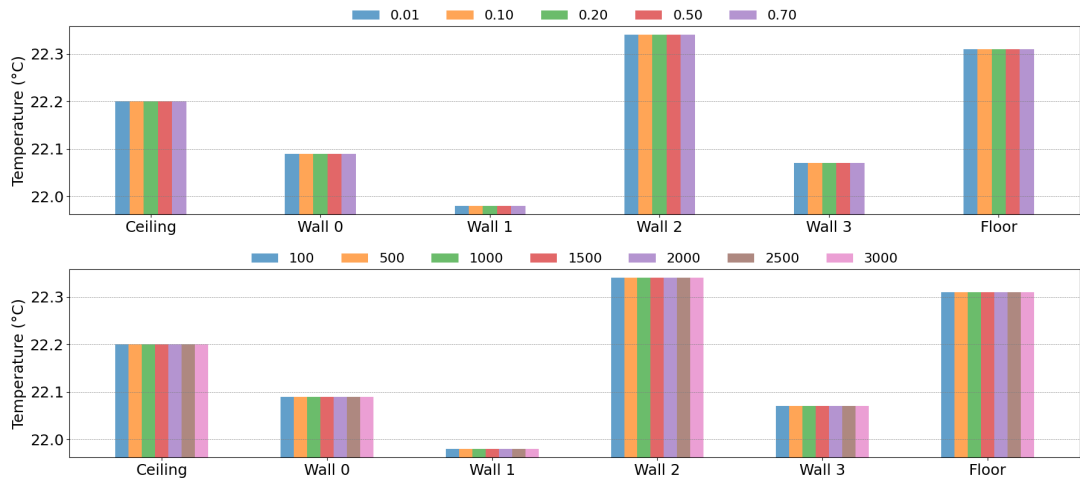


Figure 15.: (Top) The average temperature on indoor surfaces under different material conductivity values in $W/(m \cdot K)$: 0.01, 0.10, 0.20, 0.50, and 0.70. (Bottom) The average temperature on indoor surfaces under different specific heat capacity values in $J/(kg \cdot K)$: 100, 500, 1000, 1200, 2500, and 3000.

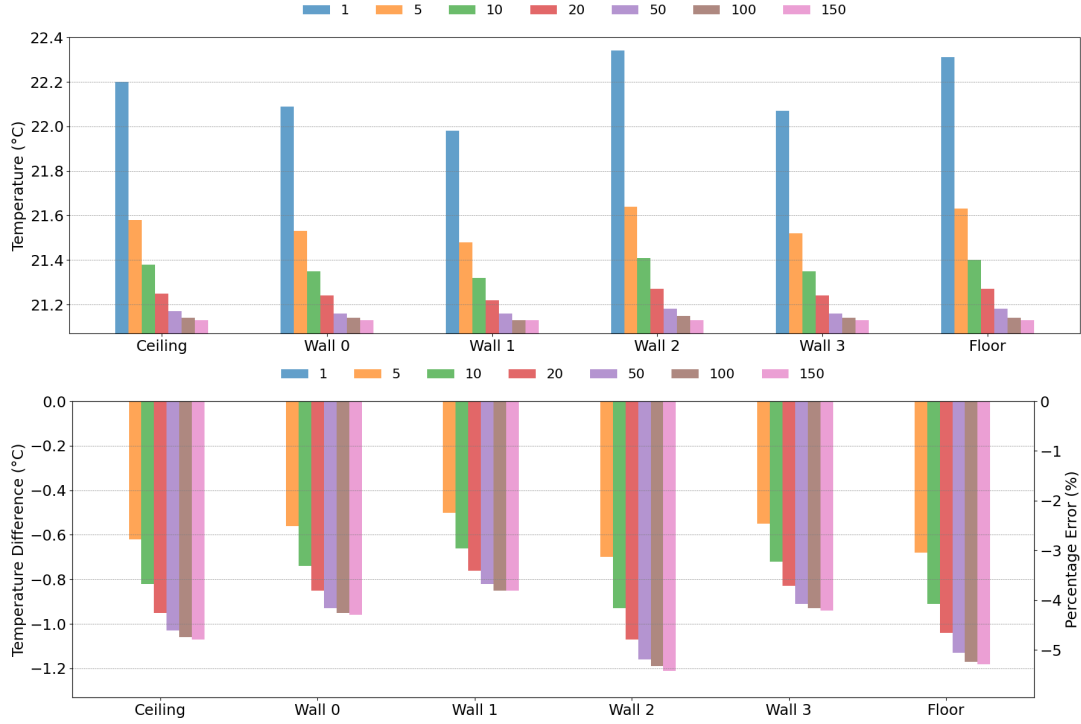


Figure 16.: (Top) The average temperature of indoor surfaces under different surface thicknesses (mm). (Bottom) Using the temperature values at the surface thickness of 1 (mm) as baseline values to compute the temperature difference ($^{\circ}C$) and percentage error (%).

mass, which alters the heat capacity. Following the default simulation settings, surface thickness is adjusted to examine its impact on surface temperatures. Temperatures under different surface thicknesses and their respective differences (using the temperatures for a 1 mm surface thickness as baseline values) are visualized in Fig. 16. As the surface thickness increases from 1 mm to 150 mm , the temperature continuously decreases. For example, for the surface temperature on the ceiling, when the thickness increased from 1 mm to 5 mm , the temperature dropped from $22.2^{\circ}C$ to below $21.6^{\circ}C$. However, when the thickness increased from 50 mm to 150 mm , the temperature change was minimal. Notably, for Wall 1, there was no temperature difference observed between thicknesses of 100 mm and 150 mm . Overall, when the indoor ambient temperature is $21.11^{\circ}C$, using thicker material results in a lower indoor temperature, bringing it closer to the ambient temperature in this setting.

When there is heat transfer between indoor and outdoor surfaces, Equ. 4 is used to estimate indoor heat maps at different outdoor temperatures. Fig. 17 shows the results with and without indoor-outdoor heat transfer at various outdoor temperatures. The image without indoor-outdoor heat transfer serves as the baseline for computing temperature differences. When the indoor ambient temperature is $21.11^{\circ}C$, an outdoor temperature of $11.85^{\circ}C$ results in lower indoor surface temperatures. As the outdoor temperature rises above the indoor temperature, it leads to higher indoor surface temperatures, with greater heat transfer occurring from the outdoor environment to the indoor space. While the temperature difference is minor, using a temperature map ranging between $-0.2^{\circ}C$ and $0.2^{\circ}C$ highlights the importance of considering indoor-outdoor

temperature exchange for accurate indoor heat estimation in a real-world scenario.

4.3. Indoor Thermal Imaging

To evaluate the results of our heat simulation, we captured the real-world scenes using a Ricoh Theta Z1 camera alongside a thermal camera. The heat simulation enables visualization of indoor heat maps in the equirectangular representation, while the thermal camera provides only a 2D perspective view. Therefore, we cropped the target region from the rendered heat map and converted it into a 2D perspective with the same field of view (FOV) as the thermal camera. We then evaluated the rendered images by comparing them with the thermal images captured by the thermal camera.

As shown in Fig. 18, a Ricoh Theta Z1 camera is positioned side by side with the FLIR thermal camera at the same height, with a Macbeth color checker and a gray matte board placed within the field of view. The real-time indoor temperature is recorded on the Govee Hygrometer Thermometer (H5075), and the outdoor temperature is obtained from GPS data in the local region.

We set up the FLIR thermal camera in TLinear mode (Boson, image resolution: 640 by 512 pixels) when capturing the thermal images. However, TLinear assumes the default emissivity, atmosphere temperature, and background temperature for the scene. The thermal image captured by TLinear requires a post-process (Veitch-Michaelis (2024)) to display the correct thermal image based on the actual emissivity of the material.

The counts ($W(T_{obj})$) from the digital converter (ADC) can be expressed as:

$$W(T_{obj}) = \frac{R}{\exp\left(\frac{B}{T_K}\right) - F} + O \quad (5)$$

Where T_K is the thermal image captured under TLinear mode, R , B , F , and O are FLIR's constant calibration coefficients.

The flux (S) at the detector can be expressed as:

$$S = \hat{\epsilon}W(T_{obj}) + (1 - \hat{\epsilon})W(T_{back}) \quad (6)$$

Where $\hat{\epsilon}$ represents the default emissivity value, and $W(T_{back})$ is the default background temperature (a constant value).

The actual actual emissivity (ϵ) is used to compute the $W(T_{obj})$:

$$W(T_{obj}) = (S - (1 - \epsilon)W(T_{back}))/\epsilon \quad (7)$$

The thermal image, displayed with the actual material emissivity, can be computed as:

$$T_K = \frac{B}{\ln\left(\frac{R}{W(T_{obj}) - O} + F\right)} \quad (8)$$

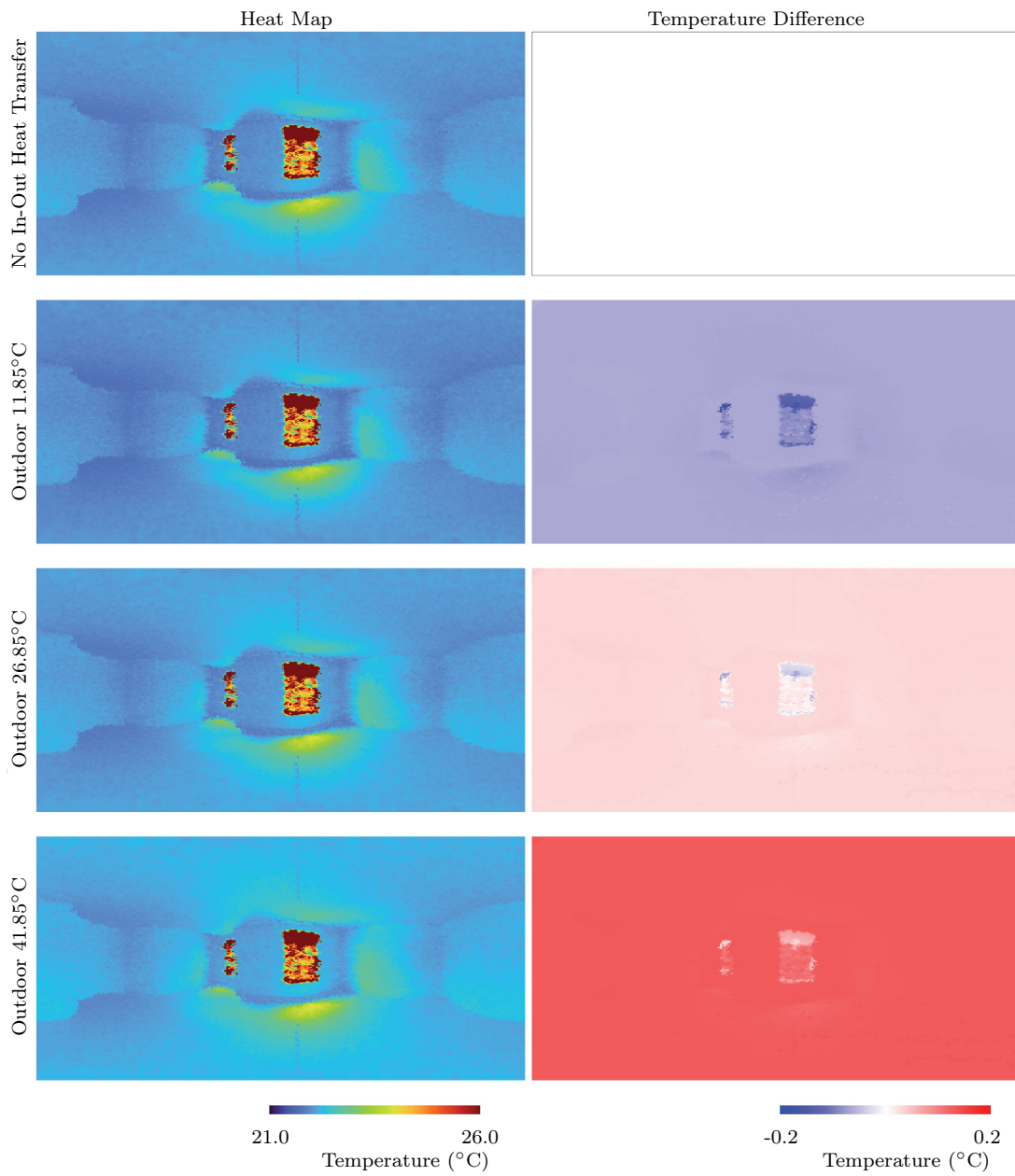


Figure 17.: Heat estimation when indoor-outdoor heat transfer is included (Equ. 4) and the indoor ambient temperature is 21.11 °C. (Left column) Heat maps under different outdoor temperatures. (Right column) Temperature differences using the heat map without indoor-outdoor heat transfer as the baseline for comparison.



Figure 18.: Camera setup for capturing indoor panorama and thermal images

4.4. Validation and Comparison

Using our proposed heat estimation method, a single indoor panorama is used to generate a panoramic heat map from the same camera position (Fig. 19). The average temperature values are calculated on the planar indoor surfaces within the white circles, and the heat estimation results are compared with the thermal images captured by the thermal camera. In Scene 1, the temperature difference at selected areas ranged from 2.00 to 2.50 °C. In Scene 2, the temperature difference was approximately 4.00 to 4.50 °C. In Scene 3, the wall plane in the upper left corner showed a temperature difference of about 1.00 °C, while the wall plane on the right and the floor exhibited larger temperature errors, close to 2.00 °C. It is also important to note that the thermal images from the thermal camera are noisy, which can lower the average temperature in the target region.

An accurate 3D floor layout is essential for precise heat estimation. We focus on the error analysis of the heat simulation in different floor layouts (Fig. 20). Layout 1 is considered as the correct floor layout, while Layouts 2 and 3 feature slight shifts in the floor boundaries. The heat maps for Layouts 2 and 3 reveal variations in indoor temperature values due to inaccuracies in the room geometry. In the Error Map, the heat maps of Layouts 2 and 3 are compared with the ground-truth (GT) heat map of Layout 1. Layout 2 shows lower temperature estimates at the upper and lower corners of the wall, while Layout 3 exhibits lower temperatures near the wall adjacent to the left window. Although the temperature differences are minor, an accurate floor layout is crucial to generate reliable indoor heat maps.

5. Conclusion

In this work, we present an application that uses paired indoor and outdoor RGB panoramas as input to estimate indoor lighting and heat properties. Built on image-based rendering techniques, our inverse rendering pipeline not only provides high-quality indoor renderings in a photorealistic manner but also enables us to estimate light levels for indoor task lighting analysis. Since the panorama provides an omnidirectional view of the scene, the task lighting tool allows users to identify suitable work areas. Besides, heat estimation is integrated with lighting analysis. The heat generated by natural light on indoor surfaces is estimated, whereas transient heat transport enables the analysis of indoor heat distribution over time. Our method provides an efficient solution for indoor lighting and thermal analysis, supporting virtual indoor staging and contributing to high-quality scene design, lighting research, and thermal

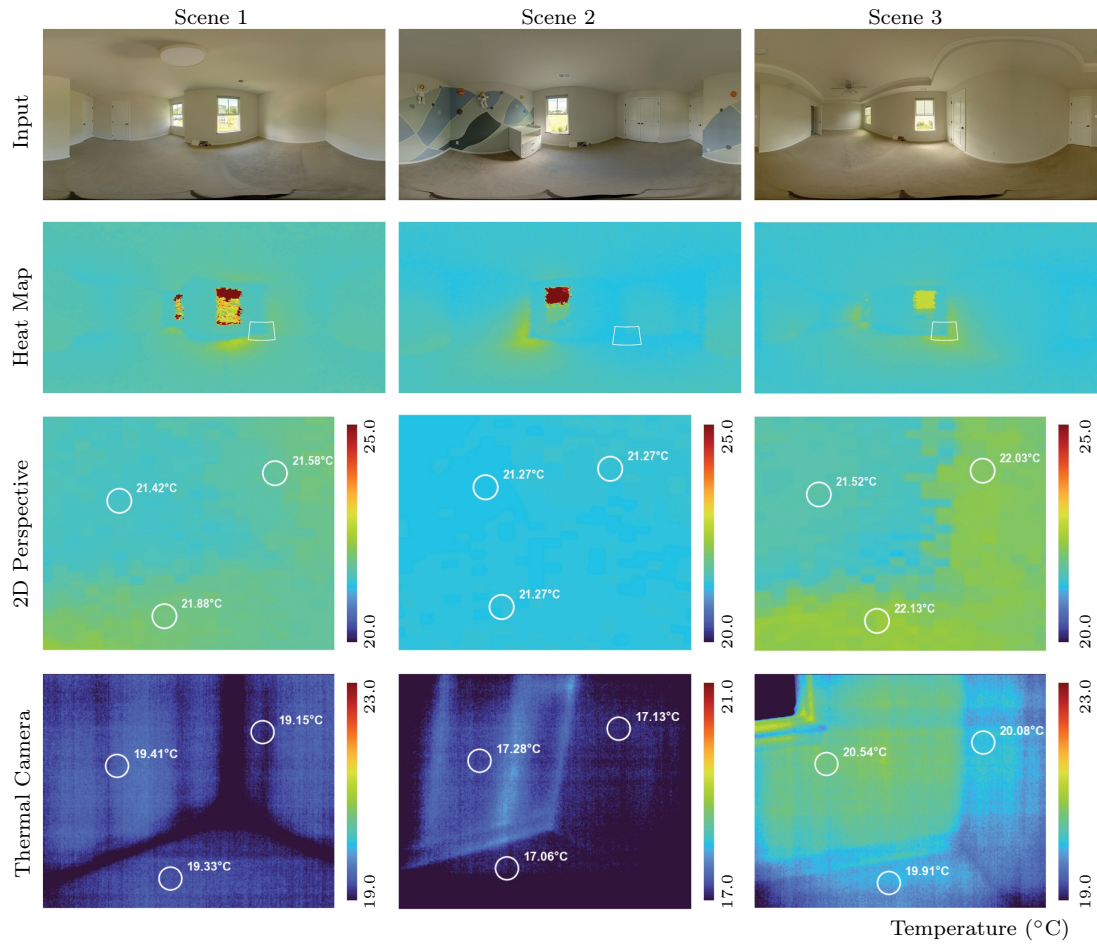


Figure 19.: Comparison between the rendered heat map and thermal images captured on-site: Three scenes were captured as inputs, and panoramic indoor heat maps were generated. The target regions were cropped to align with the thermal camera's field of view and pose. Indoor surface temperatures are highlighted in white. The temperature scale of each heat map has been adjusted for visualization.

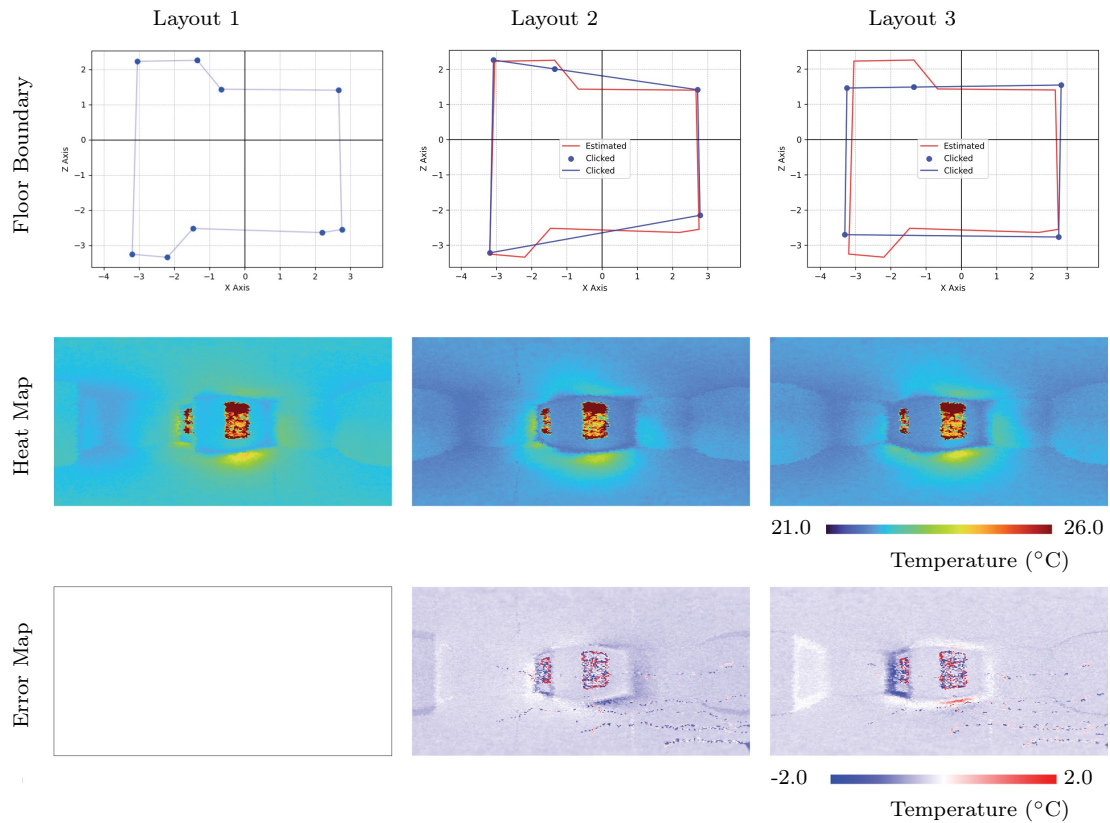


Figure 20.: Error analysis of heat estimation (Temperature ($^{\circ}\text{C}$)) for different floor layouts: Layout 1 presents the correct floor boundary, while Layouts 2 and Layout 3 edit the existing floor boundary. The Heat Map illustrates the estimated heat panoramas based on the respective floor boundaries. The Error Map uses the estimated heat map to minimize the baseline heat map from Layout 1 and displays the per-pixel temperature differences.

imaging techniques for real-world scenarios.

6. Discussion

6.1. Limitations

This paper presents the methodology for a joint estimation of light and heat for a single panorama. However, several limitations are identified in this work. The heat estimation assumes that all indoor heat originates from natural light (the outdoor RGB panorama) and takes sunlight as the sole heat source. Since mechanical systems, such as air conditioning or heating operations, are unknown in a single panorama, their power and functionality remain unknown. Consequently, the heat estimation reflects only the temperature effects caused by outdoor light. The outdoor scene is captured as a 360° environment map. This map serves as an omnidirectional illumination source from an infinite distance. However, accurately modeling detailed outdoor 3D objects can be challenging when obstructions are present. For example, under clear sky conditions, sunlight can be blocked by trees and leaves, resulting in light leakage as beams pass through the foliage. These subtle lighting effects cannot be recovered effectively, as the scene is flattened onto the environment map. The estimation of irradiance (illuminance) is based on the assumption that all objects have Lambertian surfaces. Materials such as glass or metal have not been included in this work.

6.2. Future Work

Future work should consider more complex materials, such as transparent glass and specular metals, to enhance the realism of virtual rendered scenes. Additionally, heat simulations should investigate a broader range of material properties and analyze the impacts of various parameters on heat change. Expanding the scope to include more building cases, such as those in different geographic locations, with diverse indoor materials, and under varying weather conditions, would further enrich the study and its applicability.

7. Disclosure Statement

The authors declare no potential conflicts of interest with respect to the research, authorship, and/or publication of this article.

References

- Guangzhou Ji, Azadeh O Sawyer, and Srinivasa G Narasimhan. Virtual home staging: Inverse rendering and editing an indoor panorama under natural illumination. In *International Symposium on Visual Computing*, pages 329–342. Springer, 2023.
- Guangzhou Ji, Azadeh O Sawyer, and Srinivasa G Narasimhan. Virtual home staging and relighting from a single panorama under natural illumination. *Machine Vision and Applications*, 35(4):98, 2024.
- Tiancheng Zhi, Bowei Chen, Ivaylo Boyadzhiev, Sing Bing Kang, Martial Hebert, and Srinivasa G Narasimhan. Semantically supervised appearance decomposition for virtual staging from a single panorama. *ACM Transactions on Graphics (TOG)*, 41(4):1–15, 2022.

- Paul Debevec. Image-based lighting. In *ACM SIGGRAPH 2006 Courses*, pages 4–es. Association for Computing Machinery, New York, NY, United States, 2006.
- Standard CIE. Spatial distribution of daylight-cie standard general sky. *CIE S 011.1/E*, 2003.
- Richard Perez, Robert Seals, and Joseph Michalsky. All-weather model for sky luminance distribution—preliminary configuration and validation. *Solar energy*, 50(3):235–245, 1993.
- Lukas Hosek and Alexander Wilkie. An analytic model for full spectral sky-dome radiance. *ACM Transactions on Graphics (TOG)*, 31(4):1–9, 2012.
- J Stumpfel, A Jones, A Wenger, C Tchou, T Hawkins, and P Debevec. Direct hdr capture of the sun and sky, 2004. In *ACM SIGGRAPH 2006 Courses*, pages 5–es, 2004.
- Mehlika Inanici. Applications of image based rendering in lighting simulation: Development and evaluation of image based sky models. In *Proceedings of the International IBPSA Conference, Glasgow, UK*, pages 27–30, 2009.
- Mehlika Inanici. Evaluation of high dynamic range image-based sky models in lighting simulation. *Leukos*, 7(2):69–84, 2010.
- Nicolas Bonneel, Balazs Kovacs, Sylvain Paris, and Kavita Bala. Intrinsic decompositions for image editing. In *Computer Graphics Forum*, volume 36, pages 593–609. Wiley Online Library, 2017.
- Steven M Seitz, Yasuyuki Matsushita, and Kiriakos N Kutulakos. A theory of inverse light transport. In *Tenth IEEE International Conference on Computer Vision (ICCV'05) Volume 1*, volume 2, pages 1440–1447. IEEE, 2005.
- Robert Carroll, Ravi Ramamoorthi, and Maneesh Agrawala. Illumination decomposition for material recoloring with consistent interreflections. In *ACM SIGGRAPH 2011 papers*, pages 1–10. Association for Computing Machinery (ACM), 2011.
- Sylvain Duchêne, Clement Riant, Gaurav Chaurasia, Jorge Lopez-Moreno, Pierre-Yves Laffont, Stefan Popov, Adrien Bousseau, and George Drettakis. Multi-view intrinsic images of outdoors scenes with an application to relighting. *ACM Transactions on Graphics*, page 16, 2015.
- Theodore L Bergman, Adrienne S Lavine, Frank P Incropera, and David P DeWitt. *Introduction to heat transfer*. John Wiley & Sons, 2011.
- Mani Ramanagopal, Sriram Narayanan, Aswin C Sankaranarayanan, and Srinivasa G Narasimhan. A theory of joint light and heat transport for lambertian scenes. In *Proceedings of the IEEE/CVF Conference on Computer Vision and Pattern Recognition*, pages 11924–11933, 2024.
- Marc-André Gardner, Kalyan Sunkavalli, Ersin Yumer, Xiaohui Shen, Emiliano Gambaretto, Christian Gagné, and Jean-François Lalonde. Learning to predict indoor illumination from a single image. *arXiv preprint arXiv:1704.00090*, 2017.
- Marc-André Gardner, Yannick Hold-Geoffroy, Kalyan Sunkavalli, Christian Gagné, and Jean-François Lalonde. Deep parametric indoor lighting estimation. In *Proceedings of the IEEE/CVF International Conference on Computer Vision*, pages 7175–7183, 2019.
- Vasileios Gkitsas, Nikolaos Zioulis, Federico Alvarez, Dimitrios Zarpalas, and Petros Daras. Deep lighting environment map estimation from spherical panoramas. In *Proceedings of the IEEE/CVF Conference on Computer Vision and Pattern Recognition Workshops*, pages 640–641, 2020.
- Chloe LeGendre, Wan-Chun Ma, Graham Fyffe, John Flynn, Laurent Charbonnel, Jay Busch, and Paul Debevec. Deeplight: Learning illumination for unconstrained mobile mixed reality. In *Proceedings of the IEEE/CVF Conference on Computer Vision and Pattern Recognition*, pages 5918–5928, 2019.
- Allan G Rempel, Matthew Trentacoste, Helge Seetzen, H David Young, Wolfgang Heidrich, Lorne Whitehead, and Greg Ward. Ldr2hdr: on-the-fly reverse tone mapping of legacy video and photographs. *ACM transactions on graphics (TOG)*, 26(3):39–es, 2007.
- Francesco Banterle, Patrick Ledda, Kurt Debattista, and Alan Chalmers. Inverse tone mapping. In *Proceedings of the 4th international conference on Computer graphics and interactive techniques in Australasia and Southeast Asia*, pages 349–356, 2006.
- Francesco Banterle, Patrick Ledda, Kurt Debattista, Alan Chalmers, and Marina Bloj. A

- framework for inverse tone mapping. *The Visual Computer*, 23:467–478, 2007.
- Erik Reinhard, Michael Stark, Peter Shirley, and James Ferwerda. Photographic tone reproduction for digital images. In *Proceedings of the 29th annual conference on Computer graphics and interactive techniques*, pages 267–276, 2002.
- Zhengqin Li, Jia Shi, Sai Bi, Rui Zhu, Kalyan Sunkavalli, Miloš Hašan, Zexiang Xu, Ravi Ramamoorthi, and Manmohan Chandraker. Physically-based editing of indoor scene lighting from a single image. In *European Conference on Computer Vision*, pages 555–572. Springer, 2022.
- Yu-Ying Yeh, Zhengqin Li, Yannick Hold-Geoffroy, Rui Zhu, Zexiang Xu, Miloš Hašan, Kalyan Sunkavalli, and Manmohan Chandraker. Photoscene: Photorealistic material and lighting transfer for indoor scenes. In *Proceedings of the IEEE/CVF Conference on Computer Vision and Pattern Recognition*, pages 18562–18571, 2022.
- Zhengqin Li, Mohammad Shafiei, Ravi Ramamoorthi, Kalyan Sunkavalli, and Manmohan Chandraker. Inverse rendering for complex indoor scenes: Shape, spatially-varying lighting and svbrdf from a single image. In *Proceedings of the IEEE/CVF Conference on Computer Vision and Pattern Recognition*, pages 2475–2484, 2020.
- Mathieu Garon, Kalyan Sunkavalli, Sunil Hadap, Nathan Carr, and Jean-François Lalonde. Fast spatially-varying indoor lighting estimation. In *Proceedings of the IEEE/CVF Conference on Computer Vision and Pattern Recognition*, pages 6908–6917, 2019.
- Pratul P Srinivasan, Ben Mildenhall, Matthew Tancik, Jonathan T Barron, Richard Tucker, and Noah Snavely. Lighthouse: Predicting lighting volumes for spatially-coherent illumination. In *Proceedings of the IEEE/CVF Conference on Computer Vision and Pattern Recognition*, pages 8080–8089, 2020.
- Kevin Karsch, Varsha Hedau, David Forsyth, and Derek Hoiem. Rendering synthetic objects into legacy photographs. *ACM Transactions on graphics (TOG)*, 30(6):1–12, 2011.
- Edward Zhang, Michael F Cohen, and Brian Curless. Emptying, refurbishing, and relighting indoor spaces. *ACM Transactions on Graphics (TOG)*, 35(6):1–14, 2016.
- Stanislav Darula and Richard Kittler. Cie general sky standard defining luminance distributions. *Proceedings eSim*, pages 11–13, 2002.
- Jean-François Lalonde, Alexei A Efros, and Srinivasa G Narasimhan. Estimating the natural illumination conditions from a single outdoor image. *International Journal of Computer Vision*, 98:123–145, 2012.
- Arcot J Preetham, Peter Shirley, and Brian Smits. A practical analytic model for daylight. In *Proceedings of the 26th annual conference on Computer graphics and interactive techniques*, pages 91–100, 1999.
- Yannick Hold-Geoffroy, Kalyan Sunkavalli, Sunil Hadap, Emiliano Gambaretto, and Jean-François Lalonde. Deep outdoor illumination estimation. In *Proceedings of the IEEE conference on computer vision and pattern recognition*, pages 7312–7321, 2017.
- Jean-François Lalonde and Iain Matthews. Lighting estimation in outdoor image collections. In *2014 2nd international conference on 3D vision*, volume 1, pages 131–138. IEEE, 2014.
- Jinsong Zhang and Jean-François Lalonde. Learning high dynamic range from outdoor panoramas. In *Proceedings of the IEEE International Conference on Computer Vision*, pages 4519–4528, 2017.
- Kalyan Sunkavalli, Fabiano Romeiro, Wojciech Matusik, Todd Zickler, and Hanspeter Pfister. What do color changes reveal about an outdoor scene? In *2008 IEEE Conference on Computer Vision and Pattern Recognition*, pages 1–8. IEEE, 2008.
- Mohammad Reza Karimi Dastjerdi, Jonathan Eisenmann, Yannick Hold-Geoffroy, and Jean-François Lalonde. Everlight: Indoor-outdoor editable hdr lighting estimation. In *Proceedings of the IEEE/CVF International Conference on Computer Vision*, pages 7420–7429, 2023.
- Gerald C Holst. Common sense approach to thermal imaging. (*No Title*), 2000.
- Herbert Kaplan. *Practical applications of infrared thermal sensing and imaging equipment*, volume 75. SPIE press, 2007.
- Michael Vollmer. Infrared thermal imaging. In *Computer Vision: A Reference Guide*, pages 1–4. Springer, 2020.

- Gorazd Planinsic. Infrared thermal imaging: Fundamentals, research and applications, 2011.
- Dong Huo, Jian Wang, Yiming Qian, and Yee-Hong Yang. Glass segmentation with rgb-thermal image pairs. *IEEE Transactions on Image Processing*, 32:1911–1926, 2023.
- Gonen Eren, Olivier Aubreton, Fabrice Meriaudeau, LA Sanchez Secades, David Fofi, A Teoman Naskali, Frederic Truchetet, and Aytul Ercil. Scanning from heating: 3d shape estimation of transparent objects from local surface heating. *Optics express*, 17(14):11457–11468, 2009.
- Ukcheol Shin, Jinsun Park, and In So Kweon. Deep depth estimation from thermal image. In *Proceedings of the IEEE/CVF Conference on Computer Vision and Pattern Recognition*, pages 1043–1053, 2023.
- Sriram Narayanan, Mani Ramanagopal, Mark Sheinin, Aswin C Sankaranarayanan, and Srinivasa G Narasimhan. Shape from heat conduction. In *European Conference on Computer Vision*, pages 426–444. Springer, 2025.
- Aniket Dashpute, Vishwanath Saragadam, Emma Alexander, Florian Willomitzer, Aggelos Katsaggelos, Ashok Veeraghavan, and Oliver Cossairt. Thermal spread functions (tsf): Physics-guided material classification. In *Proceedings of the IEEE/CVF Conference on Computer Vision and Pattern Recognition*, pages 1641–1650, 2023.
- Soroush Motayyeb, Farhad Samadzedegan, Farzaneh Dadrass Javan, and Hamidreza Hosseinpour. Fusion of uav-based infrared and visible images for thermal leakage map generation of building facades. *Heliyon*, 9(3), 2023.
- Małgorzata Jarzabek-Rychard, Dong Lin, and Hans-Gerd Maas. Supervised detection of façade openings in 3d point clouds with thermal attributes. *Remote Sensing*, 12(3):543, 2020.
- Antonio Adán, T Prado, Samuel A Prieto, and Blanca Quintana. Fusion of thermal imagery and lidar data for generating tbim models. In *2017 Ieee Sensors*, pages 1–3. IEEE, 2017.
- Robert Schmoll, Sebastian Schramm, Tom Breitenstein, and Andreas Kroll. Method and experimental investigation of surface heat dissipation measurement using 3d thermography. *Journal of Sensors and Sensor Systems*, 11(1):41–49, 2022.
- I Garrido, S Lagüela, and P Arias. Autonomous thermography: towards the automatic detection and classification of building pathologies. In *Proceedings of the 14th Quantitative InfraRed Thermography Conference, Berlin, Germany*, pages 25–29, 2018.
- Antonio Adán, Juan García, Blanca Quintana, Francisco J Castilla, and Víctor Pérez. Temporal-clustering based technique for identifying thermal regions in buildings. In *Advanced Concepts for Intelligent Vision Systems: 20th International Conference, ACIVS 2020, Auckland, New Zealand, February 10–14, 2020, Proceedings 20*, pages 290–301. Springer, 2020.
- L López-Fernández, S Lagüela, D González-Aguilera, and H Lorenzo. Thermographic and mobile indoor mapping for the computation of energy losses in buildings. *Indoor and Built Environment*, 26(6):771–784, 2017.
- Stephen Vidas, Peyman Moghadam, and Michael Bosse. 3d thermal mapping of building interiors using an rgb-d and thermal camera. In *2013 IEEE international conference on robotics and automation*, pages 2311–2318. IEEE, 2013.
- Xiaoming Yang, Lars Oliver Grobe, and Stephen Wittkopf. Multi-point simultaneous illuminance measurement with high dynamic range photography. In *Proceedings of International Conference CISBAT 2013: Cleantech for Smart Cities & Buildings-from Nano to Urban Scale*, volume 1, pages 347–352. EPFL, 2013.
- Peter R Michael, Danvers E Johnston, and Wilfrido Moreno. A conversion guide: solar irradiance and lux illuminance. *Journal of Measurements in Engineering*, 8(4):153–166, 2020.
- IESVE. Table 6 Thermal Conductivity, Specific Heat Capacity and Density — help.iesve.com. https://help.iesve.com/ve2018/table_6_thermal_conductivity_specific_heat_capacity_and_density.htm, 2018. [Accessed 30-10-2024].
- Josh Veitch-Michaelis. Thermal cameras; flirpy documentation — flirpy.readthedocs.io. https://flirpy.readthedocs.io/en/latest/getting_started/cameras.html#radiometry, 2024. [Accessed 14-11-2024].